Volume 1 | Number 1 | Jan 2013 | Pages 1–100

PCCP

Physical Chemistry Chemical Physics
www.rsc.org/pccp

ROYAL SOCIETY OF CHEMISTRY

ROYAL SOCIETY OF CHEMISTRY

www.rsc.org/pccp

PCCP

ARTICLE

Morphological effects of the nanostructured ceria support on the activity and stability of CuO/CeO₂ catalysts for the water-gas shift reaction

S.Y. Yao,[a,b] W.Q. Xu,[b] A.C. Johnston-Peck,[c] F.Z. Zhao,[b] Z.Y. Liu,[b,e] S. Luo,[b,e] S.D. Senanayake,[b] A. Martínez-Arias,[d] W.J. Liu*[a] and J.A. Rodriguez*[b,e]

Three CuO/CeO₂ catalysts with different morphologies of ceria, namely nanospheres, nanorods and nanocubes, were synthesized and used to catalyze the water-gas shift (WGS) reaction. The reactivity tests showed that the Cu supported on the ceria nanospheres exhibited both the highest activity and superior stability when compared with the nanocube and nanorod ceria catalysts. *Operando* X-ray diffraction (XRD), X-ray absorption fine structure (XAFS) and diffuse reflectance Fourier transform infrared spectroscopy (DRIFTS) methods were used to characterize these catalysts in their working state. High resolution electron microscopy (HRTEM, STEM) was used to look at the local atomic structure and nano-scale morphology. Our results show that the morphology of the ceria support, which can involve different crystal faces and concentrations of defects and imperfections, has a critical impact on the catalytic properties and influences: (1) the dispersion of CuO in the as-synthesized catalyst; (2) the particle size of metallic Cu upon reduction during the WGS reaction, (3) the stability of the metallic Cu upon variations of temperature, and (4) the dissociation of water on the ceria support. The nanosphere ceria catalyst showed an excellent water dissociation capability, the best dispersion of Cu and a strong Cu-Ce interaction, therefore delivering the best performance among the three WGS catalysts. The metallic Cu, which is the active species during the WGS reaction, was more stabilized on the nanospheres than on the nanorods and nanocubes and thus led to a better stability of the nanosphere catalyst than the other two architectures. Each catalyst exhibited a distinctive line-shape in the 800-1600 cm-1 region of the DRIFTS spectra, pointing to the existence of different types of carbonate or carboxylate species as surface intermediates for the WGS.

Introduction

The water-gas shift reaction (WGS, CO + H₂O → CO₂ + H₂), is one of the essential steps for hydrogen production/purification [1] and also an important reaction for reducing the CO/H₂ ratio of syngas [2]. It is thus the subject of continuous interest in industrial and academic research [3, 4-9]. Currently, the WGS processes applied in industry include the high-temperature (HT-WGS) and low-temperature shift (LT-WGS) processes which employ FeOₓ-CrOₓ and Cu/ZnO/Al₂O₃ catalysts, respectively [5, 6]. Several shortcomings of the commercial catalysts, including low efficiency, sintering, relatively high operation temperatures as well as the need of strict preconditioning and the high sensitivity of the commercial catalysts to the presence of oxygen , which make them inadequate for on-board application,

call for further research and catalyst development. Recent work indicates that Cu-CeO₂ catalysts are more active for the WGS than traditional FeOₓ-CrOₓ and Cu/ZnO/Al₂O₃ catalysts.[10,11]

Cerium oxide has been studied extensively in recent research as a dynamic functional support due to its exceptionally high oxygen storage capacity (OSC), ready reducibility, while being able to influence the redox properties of the loaded metal through synergistic effects [7]. Besides the WGS reaction [8-12], CeO₂ has also been used as a catalyst support for the oxygen-assisted WGS reaction [13-15], the preferential oxidation of CO reaction [16-18], NO reduction [19-21] and methane oxidation [22, 23].

To understand the role of ceria in catalytic reactions, model catalysts of ceria with distinct morphology and well-defined crystal faces have been studied through both experimental

This journal is © The Royal Society of Chemistry 2013

Phys. Chem. Chem. Phys., 2013, **00**, 1-3 | 1

single-crystal surface science approach [24, 25] and theoretical calculations [26-28]. Scheme 1 shows the composition of three ideal surfaces of ceria derived from its fluorite structure. The (111) and (100) are O-terminated surfaces, while the (110) exposes O and Ce centers. Recent advances in the synthesis of rare earth metal oxide nano-materials [29] enable the preparation of large quantities of ceria crystallites of a certain morphology so that the morphology effect can be studied in realistic operating conditions with powder characterization techniques. For ceria, three morphologies are most commonly synthesized and studied, including nanorods, nanocubes and nanospheres. Among the three, ceria nanorods, which mostly expose (100) and (110) faces, were reported as the best catalyst support for a range of reactions including: CO oxidation [30-32], NO reduction [33], CO_2 reforming of methane [34], preferential CO oxidation [35] and the WGS process [36]. The reasons for the ceria nanorod being a superior catalyst support were commonly attributed to the high mobility of oxygen over the (110) faces as well as a strong metal-support interaction that tends to better stabilize and anchor the metal centers. However, the methodology followed to prepare the catalysts and the nature of the metal dispersed on the ceria can affect the catalytic activity [35-37]. For instance, $Au/CeO2$ as a WGS catalyst, demonstrated that a nanorod support leads to the best catalytic performance [36]. On the other hand, in Cu-based catalysts for the WGS, polyhedral shaped ceria nanoparticles were proposed to be the best structured support [38, 39].
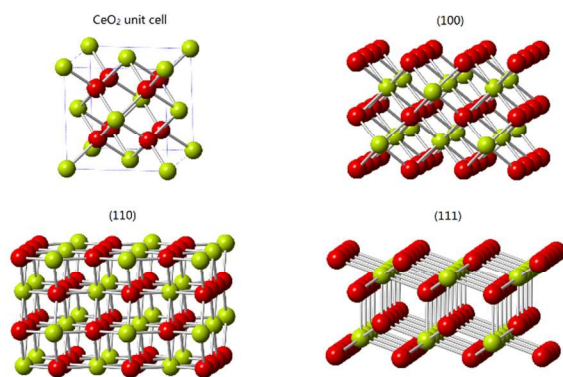
Scheme 1. Structure and composition of the (100), (110) and (111) faces of ceria

CuO/CeO_2 is one of the most widely studied nonprecious metal ceria catalysts for LT-WGS [10, 11, 38, 39]. It is believed that a strong interaction between Cu and ceria affects the WGS activity of the catalyst, but details of this interaction on different ceria crystal faces and how the different crystal faces affect the performance of the catalysts remain unclear. In this work, we examined three CuO/CeO_2 catalysts with different nanostructured ceria supports using *operando* XRD, XAFS, DRIFTS and high resolution electron microscopy (HRTEM, STEM) to clarify the relationship between the ceria morphology, the interaction between cerium oxide and copper, and the catalytic properties including the reaction mechanism of the WGS.

Experimental Section

Synthesis of CuO/CeO_2 powder catalysts

The ceria nanospheres, nanorods and nanocubes were synthesized according to procedures reported in the literature [31, 40]. Ceria nanospheres were prepared by a microemulsion method. Cerium (III) nitrate was introduced in a reverse microemulsion of water and n-heptane, which employed Triton X-100 as surfactant. A TMAH alkali solution was used as a precipitant. After adding the precipitant, the mixture was stirred for 24 h and then centrifuged, decanted and rinsed with methanol. The product was dried overnight at 100 ºC. Ceria nanorods and nanocubes were synthesized by a hydrothermal method. The cerium (III) nitrate precursor was dissolved in a NaOH aqueous solution with stirring. The mixture was introduced into a stainless steel autoclave and kept at 100 ºC and 180 ºC, respectively, for 24 h. The precipitants were further separated, washed and dried at 60 ºC overnight. All of three ceria supports were calcined in air at 500 ºC for 2 h after they were dried. Copper based catalysts employing the as prepared CeO_2 supports were prepared by incipient wetness impregnation using copper nitrate as precursor (5 wt.% Cu loading). The samples were dried overnight at 100 ºC and calcined in air at 500 ºC for 2 h. The three as-prepared catalysts are labeled as CuO/CeO_2 (ns), (nr) and (nc) for the nanosphere, nanorod and nanocube ceria supports, respectively. Specific surface areas (S_{BET}), as determined from N_2 adsorption isotherms, were of 72, 78 and 29 m^2g^{-1} for CuO/CeO_2 (ns), (nr) and (nc) catalysts, respectively.

In *operando* X-ray Diffraction

The time-resolved in operando X-ray diffraction measurement of the WGS reaction were performed at the X7B beamline (λ=0.3196 Å) of the National Synchrotron Light Source (NSLS) at Brookhaven National Laboratory (BNL). A 3 mg powder sample of each as-prepared catalyst was loaded into a 1.0 mm diameter amorphous silica tube, which was installed into an in-situ gas flow cell with a resistance heater placed under the silica tube[41]. The temperature of the sample was monitored by a 0.5 mm diameter thermocouple (C-type) placed inside the tube near the sample, while heating was regulated with a powersupply and Eurotherm controller. Gaseous products were recorded by a mass spectrometry (MS) residual gas analyzer (RGA) [12]. The in *operando* XRD measurements under WGS reaction conditions (1 % CO/ 3 % steam/ He, 10 ml/min gas flow rate) were performed between 100 and 350 ºC using stepwise heating and cooling with an increase of 50 ºC per step and a time span of 45 min at each temperature stage. The conversion of CO was determined based on the MS data. Two-dimensional XRD patterns were collected with a Perkin-Elmer amorphous silicon detector and the diffraction rings were integrated using the Fit2d code [42]. Lattice parameters, phase composition and particle size were determined with the Rietveld method using the GSAS package [43, 44].

In *operando* X-ray Absorption Fine Structure

2 | *Phys. Chem. Chem. Phys.*, 2012, **00**, 1-3

This journal is © The Royal Society of Chemistry 2012

Time-resolved in *operando* XAFS measurements were performed at the X19A beamline of the NSLS. Cu K edge (8979 eV) data were collected during the WGS reaction with the same *in-situ* cell, gas flow conditions and temperature programs used in the XRD measurements described earlier. The Cu K edge in fluorescence yield was recorded by a 4-channel Vortex silicon multi-cathode detector and the XANES and EXAFS spectra were analyzed using the Athena and Artemis codes within the Ifeffit package [45].

Transmission and Scanning Transmission Electronic Microscopy

The high-resolution TEM images were collected at 200 kV using a Cs-corrected (1 mm) JEOL JEM 2100F instrument. The annular dark field (ADF) scanning transmission electron microscopy (STEM) images were collected with an aberration-corrected Hitachi HD-2700C, a dedicated scanning transmission electron microscope operated at 200 kV. Both of these instruments were at the Center for Functional Nanomaterials at BNL. Powder samples were dispersed as a suspension in deionized water, sonicated for 60 s and introduced onto a Holey-C and Lacey-C grid. The samples were air dried before imaging.

In *operando* Diffuse Reflectance Infrared Fourier Transform Spectroscopy

In *operando* DRIFTS data were collected over the three as-prepared CuO/CeO₂ catalysts under the same WGS conditions as in the XRD measurements. A Bruker Equinox 55 FTIR spectrometer equipped with a modified Harrick Praying Mantis DRIFT flow cell (detailed information of the instrument can be found in reference[46]) was used to monitor and collect infrared spectra of surface species during stepwise heating and cooling procedures. About 10 mg of each sample was used for DRIFTS measurement. Each measurement started with data collection at room temperature. The sample and the cell were then heated to 100 ℃ and followed by a stepwise heating process till 350 ℃ with a 50 ℃ step size. Each temperature step was held for 1 h. The cooling process followed the reverse of the heating process. The composition of the outflow gas was analyzed by a MS-RGA instrument.

Results

Characterization of fresh catalysts: TEM, STEM, XANES, and XRD studies

Representative TEM and STEM images of the three fresh CuO/CeO₂ catalysts are shown in Figures 1 and 2. Ceria nanocubes expose (100) faces, and have an average crystallite size of around 25 nm. Ceria nanorods have an average dimension of 10 × 100 nm and expose (100) and (110) faces. Ceria nanospheres have a polyhedral shape with an average diameter of about 9 nm. It is generally accepted that the polyhedral particles typically result from truncated cuboctahedra and tend to expose diverse faces in which the

thermodynamically stable (111) faces are predominant [31, 36, 37]. For small polyhedral particles, the (111) faces are joined by regions that are rich in defects and imperfections [31,36,37]. CuO particles were not resolvable from the TEM and STEM images mainly due to the low contrast between Cu and Ce, and the high dispersion of very small particles a phenomena also noted in previous studies by Gamarra et al and Gawaade et al [37, 38].

The Cu K edge XANES spectra of all the three fresh catalysts showed features at 8986 and 8989 eV corresponding to quadrupole-allowed transitions from *1s* to *4p* levels and the adsorption edge of CuO, respectively [47], indicating that the initial phase for copper in the three catalysts was CuO.

XRD data of the three as-prepared catalysts at room temperature are shown in Figure 3. Features for both CeO₂ and CuO can be identified. Diffraction peaks at 2θ of 5.89°, 6.78°, 9.61°, 11.25° and 11.77° are indexed to the (111), (200), (220), (311) and (222) planes of face-centered cubic CeO₂ with a fluorite structure. The peaks at 7.27° and 7.90° are indexed to the (11-1) and (111) planes of monoclinic CuO. Based on XRD peak broadening, average crystallite size of the ceria nanosphere, nanorod and nanocube was estimated to be 9, 15 and 22 nm, respectively, in good agreement with the TEM results. From asymmetries in the ceria diffraction peaks we calculated the average strain in the ceria lattice [43, 44], and presented in Table 1. The average strain in the lattice reflects the extent of defects, imperfections and the confinement of the architecture. The larger the strain, the greater the concentration
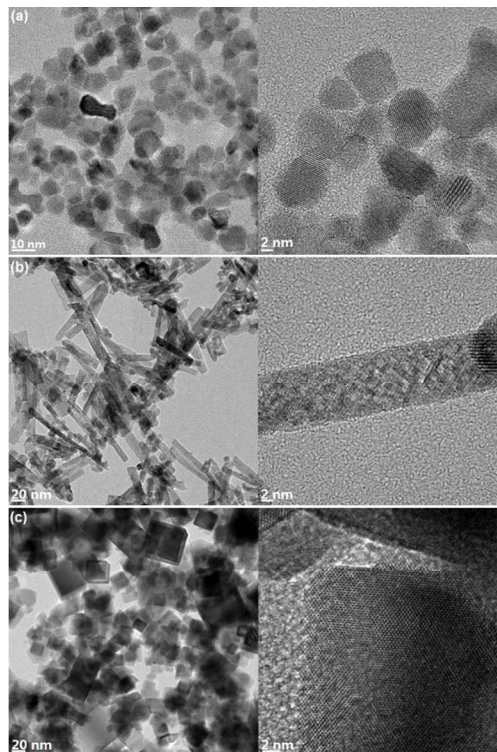

Figure 1. TEM and HRTEM images of CuO/CeO₂ (ns) (a), CuO/CeO₂ (nr) (b) and CuO/CeO₂ (nc) (c) catalysts.
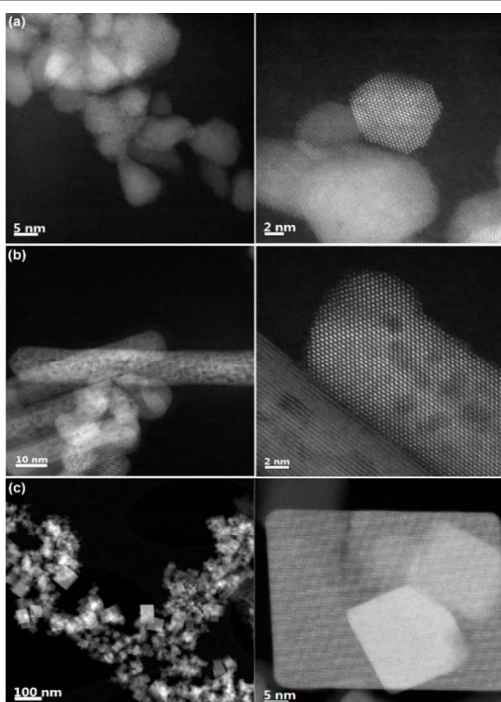
This journal is © The Royal Society of Chemistry 2012

Phys. Chem. Chem. Phys., 2012, **00**, 1-3 | **3**

Figure 2. STEM and HRSTEM images of CuO/CeO$_2$ (ns) (a), CuO/CeO$_2$ (nr) (b) and CuO/CeO$_2$ (nc) (c) catalysts.

of defects and imperfections. From the strain values in Table 1, we can conclude that the amount of defects and imperfections in the lattice of the ceria particles increases following the sequence: nanocubes < nanospheres < nanorods. As mentioned above, the specific surface areas (SBET), as determined from N$_2$ adsorption isotherms, were of 29, 72, and 78 m^{2}g^{-1} for the CuO/CeO$_2$ (nc), (ns) and (nr) catalysts, respectively. Thus, the materials with the larger specific surface areas also contain the higher concentration of defects and imperfections. Furthermore, the concentration of defects and the strain decrease with increasing particle size in Table 1. The material with the largest particle size and the lowest specific surface area has the smallest strain, i.e. the CuO/CeO$_2$ (nc) catalyst. The amount of defects and imperfections in the ceria appear to determine the dispersion of CuO by affecting the amount and type of centers for anchoring small particles on the oxide support. The nanorods have the largest amount of defects and imperfections and the smallest concentration of big particles of crystalline CuO (i.e. the highest dispersion of CuO in the form of small amorphous particles). The opposite is valid for the ceria nanocubes, which exhibit the lowest amount of defects and imperfections with the largest concentration of big particles of crystalline CuO (see Table 1). Comparing the structure and composition of the CeO$_2$(111) and CeO$_2$(100) surfaces in Scheme 1, one finds that both are O-terminated and should bind nanoparticles of CuO in a similar way. Thus, the large difference seen for the dispersion of CuO on CeO$_2$(nc) and CeO$_2$(ns) does reflect a variation in the concentration of defects and imperfections produced by the large specific surface area of CeO$_2$(ns). Certainly, in addition to predominant (111) faces in the ceria nanospheres, the presence of surface defects and

imperfections in them, as exposed above, must be taken into account when dealing with copper oxide dispersion issues in that case.
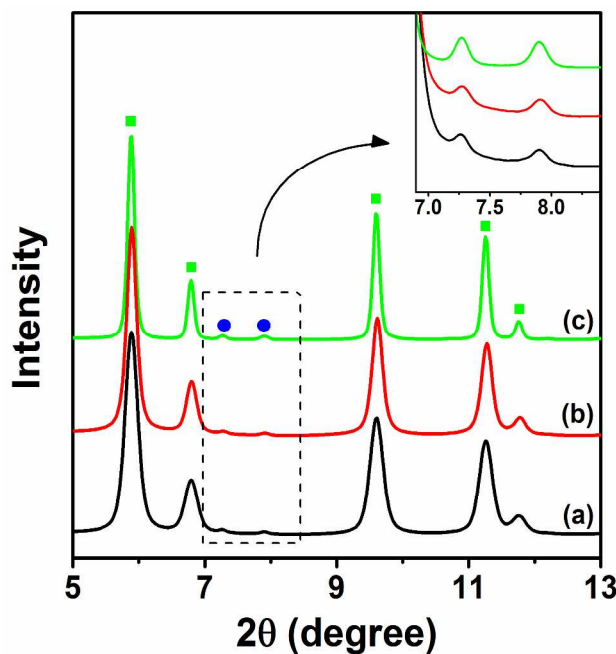

Figure 3. The XRD pattern of Ceria nanocrystal supported CuO catalysts, (a) 5 % CuO/CeO$_2$ (ns), (b) 5 % Cu/CeO$_2$ (nr) and (c) 5 % Cu/CeO$_2$ (nc).

Table 1. CeO$_2$ crystallite size, ceria lattice strain and loadings of crystalline CuO on the fresh catalysts estimated from XRD

Sample	CeO$_2$ size (nm)	strain (%)	Cryst CuO (wt.%) [a]
CuO/CeO$_2$ (ns)	9	0.39	3.1
CuO/CeO$_2$ (nr)	15	0.68	2.2
CuO/CeO$_2$ (nc)	22	0.02	6.6

[a.] Weight percentage of CuO determined by Rietveld refinement

Operando studies

A. WGS ACTIVITY AND STABILITY. *Operando* XRD, XAFS and DRIFTS were used to study the WGS reaction on the CuO/CeO$_2$ catalysts. We will start by discussing the WGS activity as measured in the micro-reactor used for the *operando* studies. These results should be understood only in relative terms since conditions applicable in such type of microreactor are not ideal ones achievable with optimized catalytic reactors. Figure 4 shows the calculated CO conversion with temperature during the two-cycle water gas shift (WGS) reaction over the three catalysts. For these measurements, we always used ~ 3mg of catalyst with a similar loading of Cu (~ 5 wt.%), as detailed in the Experimental Section. All the catalysts appeared to be active at above 200 ºC, and their activities increased with temperature. Among the three catalysts, CuO/CeO$_2$ (ns) showed the highest CO conversion equal to 64 % at 350 ºC, while CuO/CeO$_2$ (nr) and CuO/CeO$_2$ (nc) showed 53 % and 26 % conversion, respectively. A second WGS cycle, performed

subsequently with exactly the same heating and cooling procedure as in the first cycle, was performed to evaluate the stability of each catalyst. The CuO/CeO$_2$ (ns) catalyst showed the best stability with less than 1 % drop of the CO conversion at 350 ℃ in the second cycle. CO conversion over CuO/CeO$_2$ (nr) at 350 ℃ decreased to 44% in the second cycle, 9 % lower than in the first cycle. The value for CuO/CeO2 (nc) dropped to 22 % from 26 %, a loss in catalytic stability similar to that experienced by CuO/CeO$_2$ (nr), considering maximum activity level achieved in each case. Our results are in very good agreement with previous studies which indicate that CeO$_2$ (nc) is a poor support to obtain high catalytic activity [36,39]. The RGA MS data for the three CuO/CeO$_2$ catalysts are shown in the supporting information Figure S1.
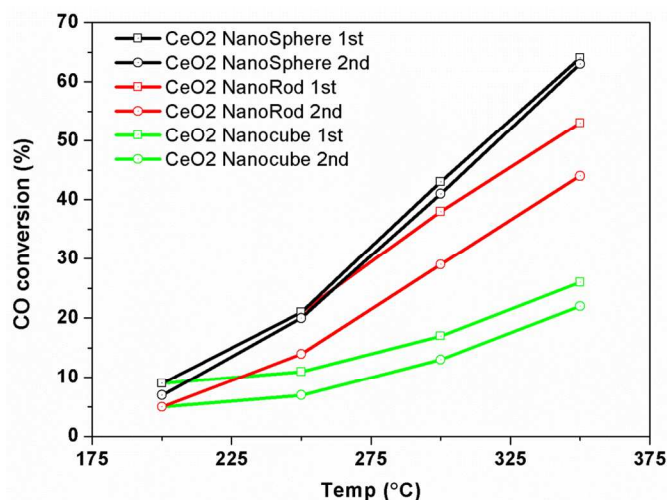

Figure 4. Water gas shift activity (calculated as CO conversion) over CuO/CeO$_2$ (ns) (black), CuO/CeO$_2$ (nr) (red) and CuO/CeO$_2$ (nc) (green) catalysts at different temperature. (□) First cycle and (○) Second cycle. Reaction conditions: [CO] = 1 %, [H$_2$O] = 3 %, gas flow rate = 10 ml/min, balanced by Helium.

B. XRD STUDIES. *In-situ* XRD proved to be an excellent tool to detect phase transformations and structural changes in the CuO/CeO$_2$ catalysts. The change of the ceria lattice constant and the amount of Cu$_2$O and Cu generated during the WGS reaction are shown in Figure 5. The values were obtained from Rietveld refinement of the *in-situ* XRD data. CuO in all three catalysts started to be reduced at 150 ℃. Details of the CuO reduction process were quite different among the three catalysts. For CuO/CeO$_2$ (ns), the CuO phase was completely reduced to metallic copper at 200 ℃ as shown in Figure 5a. At 150 ℃, a Cu$_2$O phase appeared as a metastable intermediate and disappeared by 200 ℃. The increase in metallic Cu coincided with an expansion of the ceria lattice related to a partial reduction of this oxide and the formation of a small amount of Ce(III) [10]. In contrast, for CuO/CeO$_2$ (nr), the starting CuO phase was reduced instantly to metallic Cu after the temperature reached 150 ℃ (Figure 5b). The lifetime of the intermediate Cu$_2$O, lasted for less than 10 min, which implied the major phase transformation was from CuO directly to metallic copper. For CuO/CeO$_2$ (nc), CuO showed a relatively slow reduction to Cu through Cu$_2$O. The reduction was not

practically completed until the end of the 250 ℃ temperature step, at which a residual amount of Cu$_2$O is still present. From 150 ℃ to 200 ℃, the amount of Cu$_2$O remained at a constant
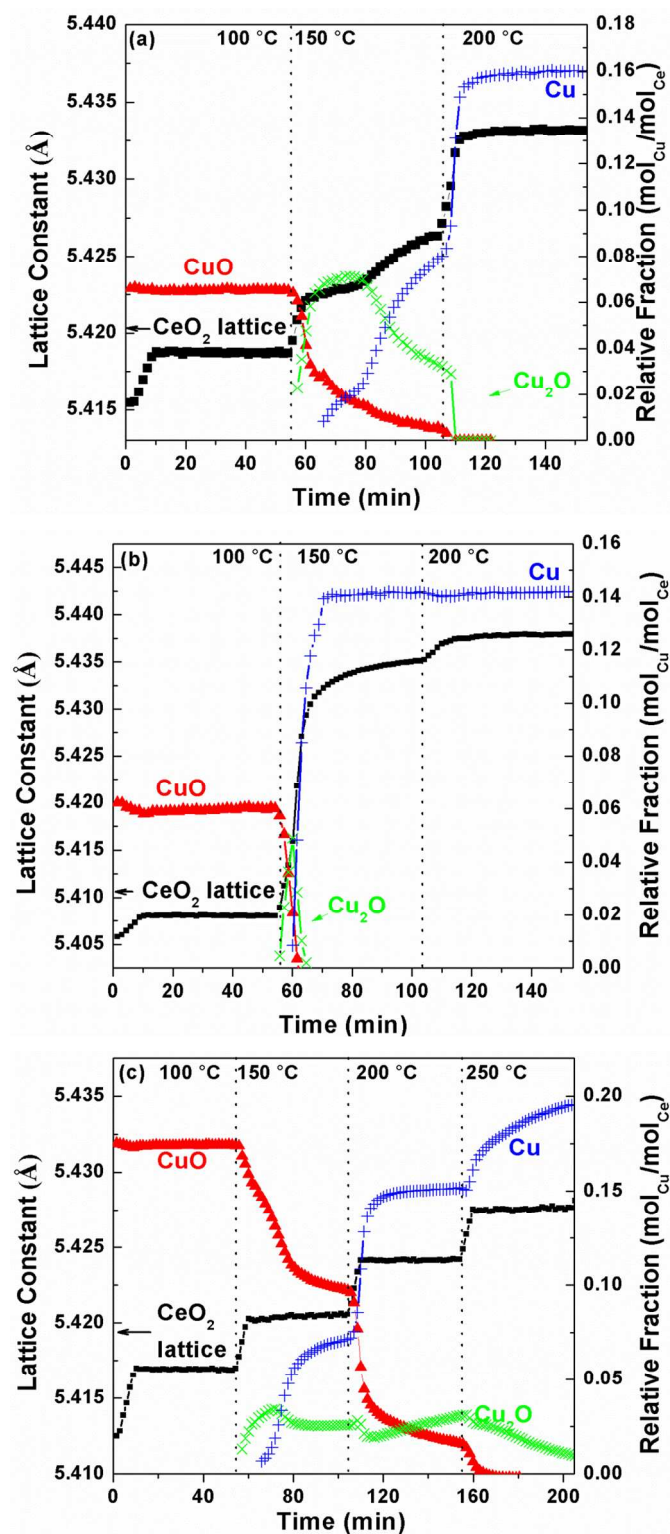

Figure 5. CeO$_2$ lattice constant and relative phase fraction of three copper species calculated using Rietveld refinement of the *in-situ* XRD data for (a) CuO/CeO$_2$ (ns), (b) CuO/CeO$_2$ (nr) and (c) CuO/CeO$_2$ (nc) catalysts.

This journal is © The Royal Society of Chemistry 2012

Phys. Chem. Chem. Phys., 2012, **00**, 1-3 | **5**

level and only began to decrease slowly at 250 °C until practically full copper reduction is attained after ca. 50 min at this temperature. The quantities of CuO, Cu_2O and metallic Cu in Figure 5 are shown relative to the abundance of CeO_2, since the total amount of the oxide support did not change throughout the experiment. For CuO/CeO_2 (ns) and CuO/CeO_2 (nr), the amount of the final metallic Cu phase was more than twice the amount of the crystalline CuO in the fresh samples (Figures 5a and b, and Table 1). The imbalance of Cu can be explained by the presence of highly dispersed small CuO particles in the starting samples which do not have long-range order and cannot be detected by XRD. These small CuO particles then become agglomerated when reduced, to form an XRD observable metallic copper phase. On the contrary, in the CuO/CeO_2 (nc) catalyst, the total amount of copper only had a slight increase during the reduction (Figure 5c) since the CuO in the fresh catalyst was dominated by crystalline CuO (Table 1). The quantities of CuO and Cu in the fresh and the reduced samples are presented in Tables 1 and 2. The weight percentage of crystalline CuO (XRD visible) is 3.1% in CuO/CeO_2 (ns) and is 2.2 % in CuO/CeO_2 (nr) (Table 1), which equals to 2.5% Cu and 1.8% Cu, much less than the 5% nominal loading amount of Cu in the synthesis. Upon reduction, the amount of copper in both samples reached 5%.

The evolution of the ceria lattice constant of the three catalysts during the WGS reaction is displayed in Figure 6. Ceria in Cu/CeO_2 (ns) and (nr) exhibited large lattice expansion from 100 °C to 200 °C besides that occurring from thermal expansion (estimated as $\approx 6.3 \times 10^{-5}$ Å K^{-1} for pure ceria in the temperature range under analysis [7]), which implied that the ceria was reduced during this period [12]. The ceria support of CeO_2 (nc) showed little extra lattice expansion other than that attributed to thermal expansion. The increase of the lattice constant which exceeds that expected from thermal expansion indicates formation of oxygen vacancies due to the reduction of Ce(IV) to Ce(III) [10]. Therefore, the ceria nanocubes generated much less oxygen vacancies than the nanospheres and nanorods. At 350 °C, the average lattice constant of ceria nanospheres and nanorods reached 5.442 Å, while the value for the nanocubes was only 5.434 Å, quite close to ≈ 5.433 Å expected from thermal expansion, considering the expansion coefficient indicated above. As shown in Figure 5, the ceria lattice expansion is correlated with the reduction of CuO, pointing to a synergistic effect at the copper oxide-ceria interface and providing evidence of a strong redox interaction in this sense. It appears that CuO and ceria in Cu/CeO_2 (nc) do not have as a strong redox interaction as those found on the nanospheres or the nanorods. A large crystal size, small specific surface area and less surface defects of the nanocubes could also contribute to their resistance to reduction and low oxygen exchange capacity. Indeed, a correlation between the level of ceria bulk reduction and respective lattice strain (Table 1) can be noted. This indicates that, as expected, the presence of bulk defects favors oxygen transport properties thus facilitating the reduction process. A higher difficulty for reduction of ceria nanocubes compared with ceria nanorods or nanospheres was

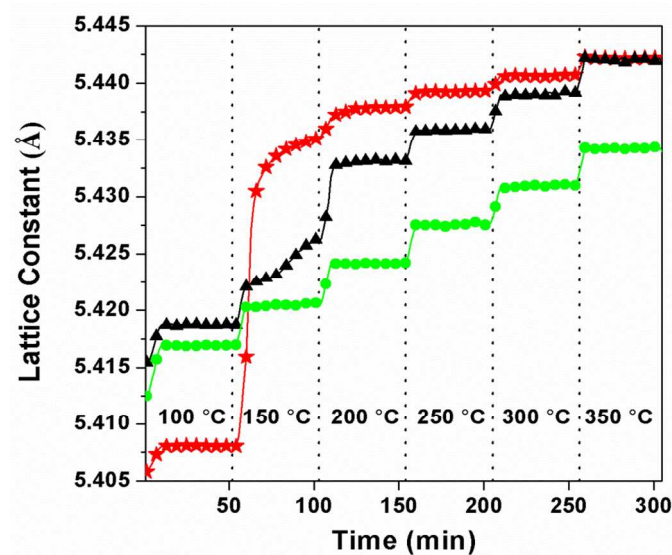also inferred recently from H_2-TPR results in CuO/CeO_2 samples with 1 wt.% Cu [37].

Figure 6. CeO_2 lattice constant in stepwise heating from room temperature to 350 °C of ▲Cu/CeO_2 (ns), ★ CuO/CeO_2 (nr) and ● CuO/CeO_2 (nc).

In the cooling process under the WGS environment, metallic copper was slightly reoxidized to Cu^+ by the water environment. A plot of the XRD patterns of the three catalysts after the first cycle was shown in the supporting material (Figure S3). Cu_2O was observed in both CuO/CeO_2 (nr) and CuO/CeO_2 (nc), but not in CuO/CeO_2 (ns). The Cu metal over the nanospheres appeared to be the most resistant to reoxidation, while the nanorod catalyst was the least resistant to oxidation.

The average crystallite sizes of the metallic Cu at 200 and 350 °C during the first cycle, and at 200 °C during the second cycle are presented in Table 2. Metallic Cu on the nanocubes

Table 2. Cu loading and the average Cu particle size of the reduced catalysts estimated from XRD

Sample	Cryst Cu (wt.%)[a]	Cu size at 200 ºC (nm)	Cu size at 350 ºC (nm)	Cu size at 200 ºC (nm)[b]
CuO/CeO_2 (ns)	6	6	6	7
CuO/CeO_2 (nr)	5	8	8	13
CuO/CeO_2 (nc)	7	20	21	22

[a]. The amount of Cu estimated by XRD are all around 5%, fairly consistent with nominal amounts and considering experimental errors both during sample synthesis and estimations made from XRD results.

[b]. For the second cycle.

has the largest particle size with a value close to 20 nm, while the corresponding values for Cu on the nanospheres and the nanorods are 6 nm and 8 nm in size, respectively. All three catalysts did not show sintering of Cu from 200 °C to 350 °C in the first WGS cycle. In the second cycle, Cu on CuO/CeO_2 (nr)

6 | *Phys. Chem. Chem. Phys.*, 2012, **00**, 1-3

This journal is © The Royal Society of Chemistry 2012

showed a dramatic growth of particle size from 8 nm to 13 nm, while Cu on the nanospheres and the nanocubes only showed a slight size increase. As will be discussed later, the main cause of the Cu particle growth is the reactant induced reduction process and not the thermal sintering of the particle.

C. XAFS STUDIES. *In situ* Cu K edge XANES experiments were performed to evaluate the redox properties of copper at different temperatures under WGS reaction conditions. Results are shown in Figure 7. The features at 8986 and 8989 eV in the Cu K edge XANES spectra of the fresh catalysts indicate the prevailing presence of CuO [47] in the samples. When the catalysts were heated to 100 ℃, the CuO/CeO_2 (nr) sample showed a small pre-edge feature at 8981 eV which could be attributed to metallic copper, indicating that CuO in the CuO/CeO_2 (nr) catalyst began to be reduced at 100 ℃, earlier than the other two catalysts. At 150 ℃, CuO/CeO_2 (nr) exhibited all the features of metallic copper. In contrast, CuO/CeO_2 (ns) still showed features due to oxidized copper at this temperature although an important reduction degree is also attained as revealed by the appreciable white line intensity decrease compared with the previous spectra at 25 and 100 ℃. In the case of CuO/CeO_2 (nc), there was a small metallic copper pre-edge feature at 150 ℃ but still an intense white line remains at this temperature thus revealing the higher difficulty for the reduction of copper in this sample. From these results, the degree of reduction sequence was CuO/CeO_2 (nr) > CuO/CeO_2 (ns) > CuO/CeO_2 (nc), which is consistent with the *in situ* XRD results discussed above. After heating to 200 ℃, the profile of the Cu K edge XANES spectra for the three catalysts was very close to that of metallic copper. Additional time-resolved XANES spectra remained unchanged for all the samples at temperatures above 200 ℃.
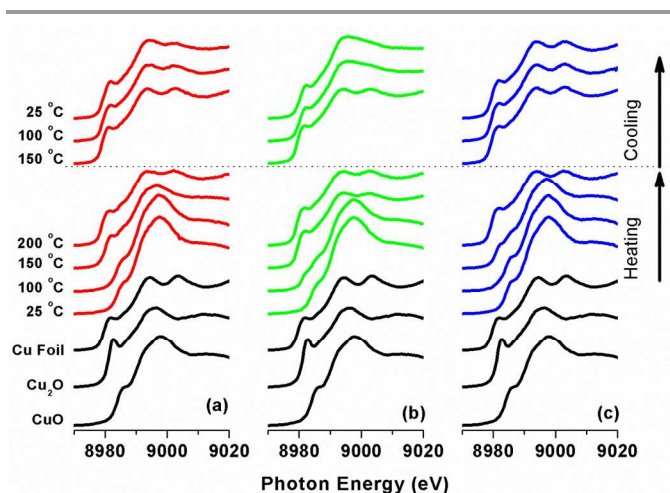
copper species in all three catalysts was still metallic copper. From 200 ℃ down to room temperature, CuO/CeO_2 (nc) showed little reoxidation, CuO/CeO_2 (ns) was slightly reoxidized by the water (as evidenced by a slight increase of the white line intensity) and CuO/CeO_2 (nr) was reoxidized strongly, especially when the system was cooled to 100 ℃. As a result, the tendency towards reoxidation of the metallic copper phase in the three catalysts upon cooling in the WGS mixture was: CuO/CeO_2 (ns) ≈ CuO/CeO_2 (nc) < CuO/CeO_2 (nr), in fair agreement with above exposed XRD results.

A Cu K edge EXAFS analysis was done to the fresh catalysts to investigate the local structure of the copper atoms. The results of the fitting are displayed in Figure 8 and Table 3. The radial distribution function of the three catalysts showed similar profiles for a CuO powder sample, with a first backscattering peak at 1.54 Å which could be fitted by 4 oxygen atoms with bond length around 1.96 Å and several higher coordination features which could be attributed to the contribution of Cu-O at 2.78 Å and Cu-Cu at 2.92 and 3.10 Å. Both XANES and EXAFS analysis of the fresh catalysts confirmed that the copper atoms exhibited a local environment similar to that in CuO. However, the difference in the average coordination number of first and higher coordination shells obtained from the EXAFS fitting indicates that the size and distribution of the CuO particles among the three catalysts are different. The average coordination numbers for the Cu-O shell were estimated to be 4.0 for CuO/CeO_2 (ns), 3.5 for CuO/CeO_2 (nr) and 4.1 for CuO/CeO_2 (nc), all values were very close to
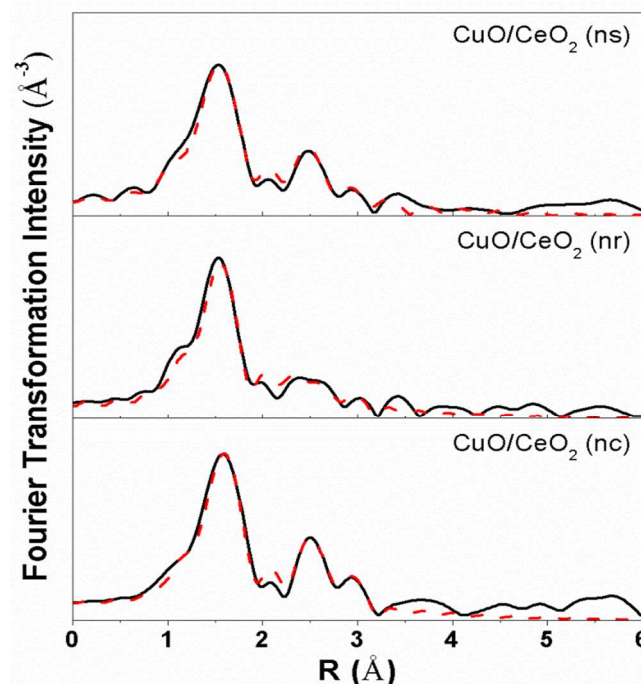

Figure 7. *In situ* Cu K edge XANES spectra of stepwise heating and cooling under WGS reaction conditions for (a) CuO/CeO_2 (ns), (b) CuO/CeO_2 (nr) and (c) CuO/CeO_2 (nc) catalysts.

Figure 8. Radial distribution function (black) and its fitting (red dash line) for the three catalysts under study.

During the stepwise cooling process, metallic copper in CuO/CeO_2 catalysts tends to be reoxidized by the water vapor in the gas feed. The reoxidation process was also monitored by XANES. When the system was cooled to 200 ℃, the observed

This journal is © The Royal Society of Chemistry 2012

Phys. Chem. Chem. Phys., 2012, **00**, 1-3 | **7**

Table 3. Results of EXAFS fitting for three copper ceria catalysts

Sample	Shell	R (Å)[a]	CN[b]	σ^2 (Å^2)[c]	E_0 shift (eV)	R factor
CuO powder	Cu-O	1.96 (1)	4	0.002 (1)	8.1	0.025
	Cu-O	2.79 (1)	2	0.002 (1)		
	Cu-Cu	2.93 (1)	4	0.003 (1)		
	Cu-Cu	3.12 (1)	4	0.003 (1)		
CuO/CeO$_2$ (ns)	Cu-O	1.95 (1)	4.0 (2)	0.003 (1)	7.5	0.010
	Cu-O	2.78 (1)	2.0 (1)	0.003 (1)		
	Cu-Cu	2.92 (1)	1.5 (1)	0.001 (1)		
	Cu-Cu	3.10 (1)	1.5 (1)	0.001 (1)		
CuO/CeO$_2$ (nr)	Cu-O	1.94 (1)	3.5 (2)	0.002 (1)	7.2	0.017
	Cu-O	2.78 (1)	1.7 (1)	0.002 (1)		
	Cu-Cu	2.92 (1)	1.1 (1)	0.003 (1)		
	Cu-Cu	3.10 (1)	1.1 (1)	0.003 (1)		
CuO/CeO$_2$ (nc)	Cu-O	1.96 (1)	4.1 (2)	0.002 (1)	12.3	0.010
	Cu-O	2.79 (1)	2.0 (1)	0.002 (1)		
	Cu-Cu	2.91 (1)	2.5 (2)	0.005 (1)		
	Cu-Cu	3.10 (1)	2.5 (2)	0.005 (1)		

[a.] Bond length

[b.] Coordination number

[c.] Debye-Waller factor

the value of the CuO standard. The relatively small value for CuO/CeO$_2$ (nr) may indicate that the CuO particles in CuO/CeO$_2$ (nr) contain more O defects and/or may be a consequence of the lower CuO crystallinity in this sample (Table 1). The average coordination number of Cu-Cu among the three catalysts are much smaller than the theoretical value of 8, indicating a lack of Cu neighbors at around 3 Å, which could be explained by the finite size of the CuO particles. As smaller metal oxides particles tend to have more unsaturated M-M coordinated atoms [48], CuO particles in the CuO/CeO$_2$ (nr) catalyst which show the smallest average coordination number for Cu-Cu shell should have the smallest average size. The smaller particle size of copper oxide in CuO/CeO$_2$ (nr) can contribute to explain why this system reduces faster than CuO/CeO$_2$ (ns) or CuO/CeO$_2$ (nc) (Figs. 5-7). The value of Cu-Cu coordination number of CuO/CeO$_2$ (ns) is about 3 and for CuO/CeO$_2$ (nc) it is around 5. This agrees with the conclusion that CuO particle size in CuO/CeO$_2$ (ns) is lower than that in CuO/CeO$_2$ (nr) but larger than that in CuO/CeO$_2$ (nc). In other words, considering the similar Cu loading in all three catalysts, the dispersion of CuO over the ceria substrates most likely

decreases following the order: CuO/CeO$_2$ (nr) > CuO/CeO$_2$ (ns) > CuO/CeO$_2$ (nc). This is in good agreement with the trend inferred from analysis of XRD results (Table 1).

D. DRIFTS STUDIES. *In situ* DRIFTS is a valuable tool for studying the WGS reaction mechanism [16, 49] and our studies showed great differences among the three catalysts in the three regions of frequency where most intense bands are detected: 3800-3000 cm^{-1}, 2150-2050 cm^{-1} and 1700-800 cm^{-1}; corresponding to O-H stretching of surface hydroxyl, C=O stretching of carbon monoxide bound to copper species and the most intense vibration modes of surface carbonates and other oxo species, respectively. Vibration frequencies and mode assignments of each band are summarized in Table 4.

Table 4. Vibration frequencies and mode assignments of adsorbed or formed species over the three CuO/CeO$_2$ catalysts [16, 49-52]

		Frequencies (cm^{-1})		
		CuO/CeO$_2$ (ns)	CuO/CeO$_2$ (nr)	CuO/CeO$_2$ (nc)
Hydroxyl	Mono-coordinated	3697	3693	3694
	Bridged-coordinated	3656	3657	3634
	Multiple-coordinated	ND [a]	3513	3604
Adsorbed CO	Cu$^+$-CO	2094	2097	2100
Oxo Species	Formate	2837	2844	2953, 2844
	Bridged carbonates	1740	ND [a]	1740
	Bi- or Tridentate carbonates	1558, 1480, 1373, 1030, 853	1576, 1468, 1366, 1080, 853	1466, 1394, 1298, 1079

[a] No detected

D.1 O-H stretching of surface hydroxyl. The evolution of surface hydroxyls on the three catalysts is as follows. CuO/CeO$_2$ (ns) showed a band at 3697 cm^{-1} when heated to 100 ºC that could be attributed to mono-coordinated hydroxyl [16, 49]. At 150 ºC, a new band appeared at 3656 cm^{-1} that could be assigned to the double bridging hydroxyl connected to two neighboring Ce atoms [16, 49]. The bridging hydroxyl appeared at the temperature when ceria lattice began to expand which suggests that the process of oxygen vacancy generation on the ceria surface favors the adsorption and dissociation of H$_2$O on those vacancy sites. At 200 ºC and above, hydroxyl bands (including that related to associated hydroxyls subjected to interaction between each other through hydrogen bonding, giving rise to the strong broad band centered at ca. 3400 cm^{-1}) strongly decreased in fair coincidence with the reduction of CuO to Cu observed in XRD and the start of the WGS reaction. This may reflect consumption of hydroxyls as a consequence of the WGS process as well as from water desorption from the sample surface. For the CuO/CeO$_2$ (nr) catalyst, a band at 3693

8 | *Phys. Chem. Chem. Phys.*, 2012, **00**, 1-3

This journal is © The Royal Society of Chemistry 2012

cm[-1] attributed to mono-coordinated hydroxyl [16, 49] could be identified at 25 ℃ and 100 ℃. At 150 ℃, this band decreased in intensity and another three bands could be observed at 3741, 3657 and 3513 cm^{-1}. The bands at 3657 and 3513 cm^{-1} can be assigned to double and triple coordinated hydroxyls, respectively [16, 49]. These two bands decreased in intensity at above 200 ℃. The band at 3741 cm^{-1} was at a higher frequency than commonly found for hydroxyls on ceria. This band could also be observed on the other two catalysts but with weaker intensities, and does not change throughout the WGS process so that the species associated with this band at 3741 cm^{-1}, though not assigned in this study, did not apparently participate in the reaction. For the CuO/CeO₂ (nc) catalyst, mono- and bridging hydroxyls were observed at 3694 cm^{-1} and 3634 cm^{-1}, similar to the other two catalysts. A band at 3604 cm^{-1} appeared at above 250 ℃ when the bridging hydroxyl band at 3634 cm^{-1} disappeared. It could be associated with another type of multi-bonded hydroxyl. The cooling process obeyed the reverse sequence (see Figure S5 in the Supporting Information).

D.2 C=O stretching of adsorbed carbon monoxide. In the region of the C=O stretching of metal carbonyls, a band around 2100 cm^{-1} associated with CO bonded to Cu^{+} [50] appeared at 100 ℃ for all of the three catalysts. It needs to be noted that the Cu₂O crystalline phase did not appear until 150 ℃ according to the results of the *in situ* XRD experiments. But as indicated by DRIFTS, the surface of CuO should have been reduced to Cu^{+} at a temperature as low as 100 ℃. The intensity of the band at 2100 cm^{-1} decreased at higher temperatures when Cu^{+} was reduced to metallic copper. This band disappeared at 200 ℃ on CuO/CeO₂ (ns) and (nr) and at 250 ℃ on CuO/CeO₂ (nc). The intensity of the Cu^{+} carbonyl band reflects the amount of interfacial Cu^{+} sites [37, 51]. The CuO/CeO₂ (nc) catalyst showed an extremely strong Cu^{+} carbonyl band compared to the other two catalysts during the heating process, even though it had the least amount of Cu^{+} as estimated from XAFS. Such phenomenon was also observed by Gamarra et al. in their studies of the PROX reaction employing 1 % Cu dispersed over the same CeO₂ substrates [37]. As proposed in their paper, the interaction of CuO with CeO₂ (100) faces is much stronger than the interaction with the (111) and (110) faces of CeO₂. Therefore, Cu^{+} was more stabilized on nanocubes, which mainly exposes the (100) face, than on the nanorods and the nanospheres, therefore showed higher surface concentration as indicated by the DRIFTS spectra. Interfacial copper oxides over ceria nanospheres and nanorods tend to be more rapidly reduced to Cu (0) thus weaker Cu^{+} carbonyl bands were shown. The stability of Cu^{+} species is consistent with the XRD result which showed that the crystalline Cu₂O could still be observed at 250 ℃ on the nanocubes (Figure 5c). We found that during cooling from 350 to 25 ℃ (see Figures S5 in Supporting Information) , the Cu^{+} carbonyl band reappeared at 150 ℃ on CuO/CeO₂ (nr) and CuO/CeO₂ (nc), but did not appear until 100 ℃ on CuO/CeO₂ (ns) as a very weak band at 2095 cm^{-1}. The near absence of the regeneration of the Cu^{+} carbonyl band over the CuO/CeO₂ (ns) catalyst is most likely because metallic copper was more stabilized on the nanosphere, presenting the

least potential to be reoxidized among the three catalysts. This result is also consistent with the XRD data of the catalysts after one cycle of reaction (Figure S3 in the supporting information).

D.3 Surface carbonates and other oxo species. The evolution of carbonates and other oxo species over ceria, which showed complex features and big differences among the three catalysts, appears in the regions of 3000~2800 cm^{-1} and 1700~800 cm^{-1} [16, 52]. On the CuO/CeO₂ (ns) catalyst, the band of adsorbed water at ca. 1640 cm^{-1} decreased as the temperature was raised. A small C-H stretching band of surface formates at 2837 cm^{-1} was observed at 150 ℃ but it was not seen at temperatures above 200 ℃ when the catalyst was most active. An identical trend was seen on the nanorods and nanocubes indicating that formate is probably not a key intermediate for the WGS on all these copper-ceria catalysts. On the CuO/CeO₂(ns) catalyst, the bands at 1558, 1480, 1373, 1030 and 853 cm^{-1} could be associated to different types of bi and tridentate carbonates. The 1740 cm^{-1} band generated at 250 ℃ also suggested the existence of bridging carbonates over ceria surface at high temperature. On the CuO/CeO₂ (nr) catalyst, peaks at around 1550 and 1370~1300 cm^{-1} as well as the peaks at 1080 and 853 cm^{-1} were related to bi- and tridentate carbonates. The bridging CO band at 1740 cm^{-1} observed on the nanospheres was not observed on the nanorods but it was seen on the nanocubes. CuO/CeO₂ (nc) showed two strong bands centered at 1466 and 1394 cm^{-1} associated with carbonates adsorbed on the ceria (100) face. These bands were not seen on the CuO/CeO₂ (ns) catalyst and were present on CuO/CeO₂ (nc) in a wide range of temperature. These carbonate species are strongly bound to the nanocubes and do not participate in the catalytic process. They maybe poisons of active sites on the surface of CuO/CeO₂ (nc). A recent study has proposed an adsorbed carboxylate (CO₂[δ-]) species as a key intermediate for the WGS on a model CeO_x/Cu(111) catalyst.[53] The IR bands for such species are expected at 1200-1300 and 1600-1700 cm^{-1}. They could be present in the IR spectra of Figures 9-11, overlapping with the expected bands for carbonate species.
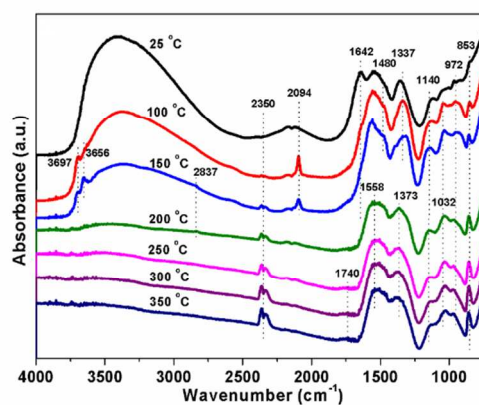

Figure 9. *In-situ* DRIFTS spectra collected during the WGS reaction over CuO/CeO₂ (ns) catalyst at different temperatures.
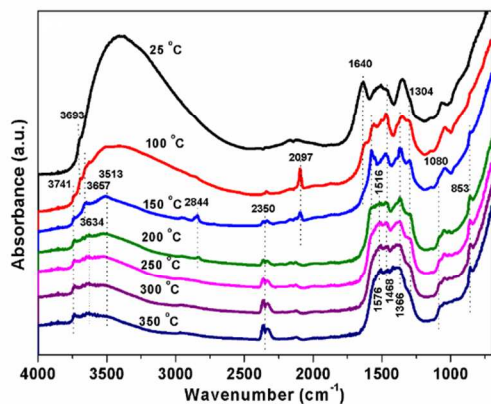
Figure 10. *In-situ* DRIFTS spectra collected during the WGS reaction over a CuO/CeO$_2$ (nr) catalyst at different temperatures.
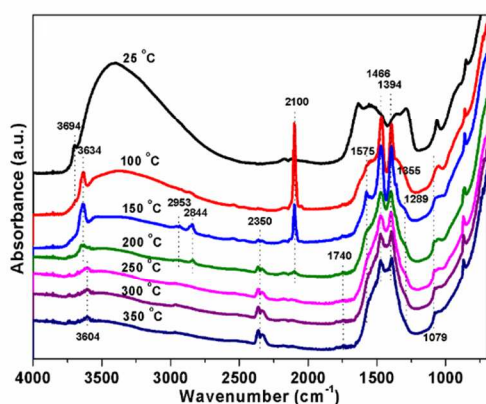

Figure 11. *In-situ* DRIFTS spectra collected during the WGS reaction over a CuO/CeO$_2$ (nc) catalyst at different temperatures.

Discussion

The performance of a catalyst can be attributed to several factors such as the concentration of active site, the size of the metal particles, and the possible cooperative interactions between the metal and support. These factors are interdependent and all can be directly or indirectly related to the surface of the support where the metals reside. In other words, the morphology of the support, which determines the most exposed crystal faces, has a critical impact on the chemical properties of the catalyst. In this study, we examined three CuO/CeO$_2$ catalysts with different particle shapes for ceria: nanocubes, nanorods and nanospheres. The nanocubes expose (100) planes, the nanorods (110) and (100), and the nanospheres multiple faces dominated by (111). In addition to exposing different faces, the ceria nanoparticles also have a different concentration of defects and imperfections in their lattices probably as a consequence of differences in preparation conditions employed in each case which are also reflected in

differences in particle size as well as specific surface areas. These differences lead to different structural and catalytic properties of the three catalysts, in the following four aspects.

1. Dispersion of CuO in the as-prepared catalysts

In the fresh CuO/CeO$_2$ (ns) and CuO/CeO$_2$ (nr) catalysts, a large amount of CuO appears as well dispersed on ceria forming very small particles invisible to XRD (< 1 nm), see Scheme 2. On the contrary, the fresh CuO/CeO$_2$ (nc) mainly has crystalline CuO. This must be a consequence of the amount of defects and imperfections present respectively in the surface of the samples, which could be extrapolated from the strain parameter derived from XRD data, as well as respective strength of the interaction of CuO with every type of exposed face present at the ceria nanoparticles [54]. It is also relevant to consider respective specific surface areas, as mentioned in Experimental about 2-3 times larger in nanorods or nanospheres than in nanocubes [37]. On the whole, ceria nanospheres and nanorods apparently favor a high dispersion of CuO in the form of small XRD-silent CuO particles, see Scheme 2. When surface sites become saturated with such highly dispersed CuO particles, the rest of the copper apparently segregates in the form of more or less big CuO crystals, globally resulting in a type of bimodal distribution of CuO particles. On the contrary, ceria nanocubes apparently favor the formation of more or less homogeneous CuO crystals basically in a monomodal distribution of the particles, in agreement with results observed on CuO/CeO$_2$ samples with 1 wt.% Cu [37]. It is relevant to note in this sense that the differences in the morphology of the dispersed CuO particles have a substantial effect on the reducibility of the system and its catalytic properties.
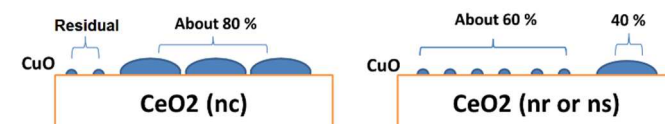
Scheme 2. Proposed structural models for CuO/CeO$_2$ catalysts based on electron microscopy, XRD and XAFS results.

2. Size of Cu during the WGS reaction

Under the WGS conditions, all CuO in the fresh catalysts, including both the crystalline part and the well dispersed part, is reduced to metallic Cu, which is the active phase for the WGS reaction. The average Cu particle size is 6 nm for CuO/CeO$_2$ (ns), 8 nm for CuO/CeO$_2$ (nr) and 20 nm for CuO/CeO$_2$ (nc). Compared with the highly dispersed state of CuO present in fresh CuO/CeO$_2$ (ns) and CuO/CeO$_2$ (nr), the formed Cu metal particles appear of relatively large size. This is expected as the interaction between a metal and an oxide is not as strong as the oxide-oxide interaction. Thus, a reduction process usually leads to particle growth. Nevertheless, the extent of growth could be different depending on the type of face exposed by ceria. Recently, Weixue Li and coworkers suggested the metal particle growth on an oxide surface could be analogous to the infiltration of liquid into a solid surface [54]. According to their

10 | *Phys. Chem. Chem. Phys.*, 2012, **00**, 1-3

This journal is © The Royal Society of Chemistry 2012

study, the relative intensity of the surface energy of the metal-gas interface γ_{mg}, the metal-oxide interface γ_{mo} as well as the oxide-gas interface γ_{og} can influence the contacting angle of the metal particle. For the same metal dispersed over different faces of an oxide, the term γ_{mg} does not change, thus the wetting angle will be determined by the difference between γ_{mo} and γ_{og}. Generally speaking, the stronger the metal-support interaction, the smaller the average particle size will be. The presence of defects and imperfections in the ceria substrate should facilitate a strong metal-support interaction, therefore the CuO/CeO_2 (ns) and the CuO/CeO_2 (nr) maintain smaller Cu particle size under reaction conditions. We cannot however discard that the lower specific surface area of ceria nanocubes could also play a relevant role on achievement of largest size in the metallic copper particles under WGS conditions.

3. Stabilization of metallic Cu

As metallic Cu(0) is the active phase for the WGS reaction, retaining Cu(0) from being re-oxidized would be preferred for a good WGS catalyst. Another reason for stabilizing Cu(0) is to avoid particle growth in repeated reduction/oxidation cycles. When cooling in the WGS environment, reoxidation of metallic copper to Cu (I) occurred in all three catalysts but to different extent. Cu/CeO_2 (ns) only had slight surface reoxidation, while the Cu/CeO_2 (nr) showed significant oxidation to bulk Cu_2O indicated by the XANES and XRD study. The lower stability of the metallic copper particles on nanorods appears also reflected in the large growth of the Cu particle size and the decreased activity observed during the second cycle of the *in situ* XRD experiments on this sample. The different extent of reoxidation can be attributed to the relative oxygen affinity of the Ce (III) site over different ceria crystal faces. Among the three faces of ceria including (100), (110) and (111), the (111) face has the largest oxygen vacancy formation energy and it tends to quickly fix its defects by grabbing oxygen from the water molecule [26, 27, 36]. Therefore, the (111) face has the lowest oxygen mobility and thus is the least likely to transfer oxygen to oxidize the copper, irrespective of whether such particles become more favorably stabilized at defective sites of the nanospheres than at predominant (111) terraces. On the contrary, the (110) face has the least oxygen vacancy formation energy and the highest surface oxygen mobility and tends to oxidize the metallic copper easily. As a result, the Cu/CeO_2 (ns) showed the most stabilized metallic Cu phase which contributed to the stability of this catalyst.

4. Water dissociation on ceria

Water dissociation is a critical step in the WGS reaction. Extended surfaces and nanoparticles of copper are not very efficient for the dissociation of water [55, 56]. The ceria support and the copper-ceria interface can help with the dissociation of water during the WGS reaction [57]. Water adsorbs dissociatively on both $CeO_2(100)$ and $CeO_2(111)$, but interacts better with the $CeO_2(100)$ surface [58]. This trend, however, can be modified when O vacancies and defects are present on the ceria surfaces [58, 59]. Ceria in general has a good oxygen exchange capacity, as

the Ce(IV) can be reduced to Ce(III) by CO thus creating vacant oxygen sites. This process is even enhanced by the supported Cu metal and can be recorded by XRD since the partial reduction of Ce(IV) to Ce(III) leads to an expansion of the ceria fcc cell lattice [12]. As shown in Figure 6, both Cu/CeO_2 (ns) and (nr) displayed a large extra lattice expansion from 100 ºC to 200 ºC, while CeO_2 (nc) only showed thermal expansion. In fact, Cu/CeO_2 (nr) showed even larger and more rapid expansion than Cu/CeO_2 (ns) at 150 ºC. The ceria lattice expansion curves correlate well with CuO reduction curves in Figure 5 and the amount of the dispersed CuO in the fresh samples, which could be taken as evidence of a strong metal-support interaction. Apparently, Cu/CeO_2 (nc) does not have a metal-support interaction as strong as in the Cu/CeO_2 (nr) or the Cu/CeO_2 (ns). Thus, during the WGS reaction, both Cu/CeO_2 (nr) and Cu/CeO_2 (ns) are inferred to exhibit plenty of O vacancy sites for water dissociation. In turn, in contrast to nanocubes, the large specific surface areas of the nanorods and nanospheres also favor a substantial concentration of defects and imperfections which does favor interaction with water [59]. Furthermore, since the dispersion of Cu is larger on the nanorods and nanospheres, the perimeter of the copper-ceria interface should be larger on Cu/CeO_2 (nr) and Cu/CeO_2 (ns) than on Cu/CeO_2 (nc), also favoring dissociation of water through synergistic interactions between copper and ceria [57].

WGS performance as a function of CeO_2 morphology

The WGS activity and stability of CuO/CeO_2 (ns) are both the best in our evaluation. We attribute the superior performance of this catalyst to a special combination of the morphological properties of the support, achievement of a reasonably small Cu particle size and a strong metal-support interaction which favors metal-support redox interplay. With regards to activity, the CuO/CeO_2 (ns) catalyst exhibits a large ceria lattice expansion which suggests the formation of sufficient Ce(III) sites for water dissociation [10, 11]. Meanwhile, the large Cu-CeO_2 interface surface energy over the ceria nanospheres constrains the particle size of metallic copper upon the reduction of CuO. As a result, this catalyst possesses the largest Cu-CeO_2 interface among the three catalysts. Such structural advantages enhance the transformation of water to surface hydroxyl species and increase the WGS reaction activity. With regards to stability, it is clear that the decrease of activity in the second WGS reaction cycle is related to the growth of the Cu particle size. The increased growth mostly occurred during the reduction process. The ceria (111) face has a strong oxygen affinity and low oxygen mobility that helps to stabilize the Cu(0) state during the cooling cycle, therefore limiting the growth of the Cu particles and sustaining the catalytic performance. The situation for CuO/CeO_2 (nr) is interesting in the sense that it apparently displays the highest dispersion in the initial oxidized state (as inferred from XRD and XAFS) and in principle the highest concentration of oxygen vacancies during WGS reaction. However, it displays lower activity than CuO/CeO_2 (ns). In this respect, from the results obtained, it appears clear that the size achieved by active metallic copper

particles under the WGS atmosphere (which must in principle determine the amount of interfacial sites present in each case) basically determine the WGS activity in each case. The difference between ceria nanospheres and nanorods appears therefore related to the degree of stabilization of metallic copper nanoparticles and this can in turn be associated, in addition to differences in oxygen dynamics as exposed above, to the respective density of surface defects present in each case. Contrary to those two samples, the sample supported on ceria nanocubes exhibit a number of factors which result detrimental in relative terms for its WGS activity: large metallic copper particles, low concentration of oxygen vacancies and a trend to stabilize partially reduced Cu(I) state less active than metallic copper for the WGS reaction; the stabilization of particular carbonate species on the (100) face of ceria, on the basis of the DRIFTS experiments shown in Fig. 11, could also play a negative role on the activity of this catalyst.

Conclusions

Three nanostructures of CeO_2 with different morphologies (spheres, rods and cubes) were synthesized and used as supports for Cu in the WGS reaction. CuO/CeO_2 (ns) was the best among the three studied catalysts with regard to both activity and stability. CuO/CeO_2 (nr) had slightly lower activity than CuO/CeO_2 (ns) and worse stability. On the other hand, CuO/CeO_2 (nc) had poor activity and moderate stability. Multiple *in-situ* characterization methods including XRD, XAFS and DRIFTS as well as electron microscopy were applied to find the most probable causes behind these differences. It was found that the concentration of defects and imperfections in the ceria support had a marked effect on the dispersed state of the deposited CuO and the particle size of the Cu metal generated during the WGS reaction, greatly influencing the performance of the catalyst. The stability of the catalysts was inversely related to the growth of metallic Cu particles, which occurs during the reduction process taking place under the WGS atmosphere. The presence of defects and imperfections in the oxide support favored strong metal-support interactions which helped to give the CuO/CeO_2 (ns) catalyst high activity and stability. In any case, a correlation is found between the size of metallic copper particles formed under WGS atmosphere in the course of the reaction (which in turn must determine the amount of interfacial active sites) and the WGS activity achieved in each case. Such effect as well as respective stability of the catalysts are correlated with the type of surface and/or surface defects present in each case as well as with differences in specific surface area between the examined samples. In turn, the results of DRIFTS indicated that formate was not a key intermediate for the WGS reaction on the three CuO/CeO_2 catalysts investigated while specific carbonate species could also act as poisons of active sites on the surface of CuO/CeO_2 (nc).

Acknowledgement

Notes and references

1. E. D. Park, D. Lee and H. C. Lee, *Catalysis Today*, 2009, **139**, 280-290.
2. R. M. Navarro, M. A. Pena and J. L. Fierro, *Chemical reviews*, 2007, **107**, 3952-3991.
3. R. Burch, *Physical chemistry chemical physics : PCCP*, 2006, **8**, 5483-5500.
4. C. Ratnasamy and J. P. Wagner, *Catalysis Reviews*, 2009, **51**, 325-440.
5. G. C. de Araújo and M. do Carmo Rangel, *Catalysis Today*, 2000, **62**, 201-207.
6. H. Yahiro, K. Murawaki, K. Saiki, T. Yamamoto and H. Yamaura, *Catalysis Today*, 2007, **126**, 436-440.
7. A. Trovarelli, *Catalysis Reviews*, 1996, **38**, 439-520.
8. Q. Fu, H. Saltsburg and M. Flytzani-Stephanopoulos, *Science*, 2003, **301**, 935-938.
9. T. Bunluesin, R. J. Gorte and G. W. Graham, *Applied Catalysis B: Environmental*, 1998, **15**, 107-114.
10. X. Wang, J. A. Rodriguez, J. C. Hanson, D. Gamarra, A. Martinez-Arias and M. Fernandez-Garcia, *The journal of physical chemistry. B*, 2006, **110**, 428-434.
11. L. Barrio, M. Estrella, G. Zhou, W. Wen, J. C. Hanson, A. B. Hungría, A. Hornés, M. Fernández-García, A. Martínez-Arias and J. A. Rodriguez, *The Journal of Physical Chemistry C*, 2010, **114**, 3580-3587.
12. W. Xu, R. Si, S. D. Senanayake, J. Llorca, H. Idriss, D. Stacchiola, J. C. Hanson and J. A. Rodriguez, *Journal of Catalysis*, 2012, **291**, 117-126.

13. E. S. Bickford, S. Velu and C. Song, *Catalysis Today*, 2005, **99**, 347-357.

14. E. B. Fox, S. Velu, M. H. Engelhard, Y.-H. Chin, J. T. Miller, J. Kropf and C. Song, *Journal of Catalysis*, 2008, **260**, 358-370.

15. E. B. Fox, A. F. Lee, K. Wilson and C. Song, *Topics in Catalysis*, 2008, **49**, 89-96.

16. O. Pozdnyakova, D. Teschner, A. Wootsch, J. Krohnert, B. Steinhauer, H. Sauer, L. Toth, F. Jentoft, A. Knopgericke and Z. Paal, *Journal of Catalysis*, 2006, **237**, 1-16.

17. D. Gamarra, C. Belver, M. Fernandez-Garcia and A. Martinez-Arias, *Journal of the American Chemical Society*, 2007, **129**, 12064-12065.

18. G. Panzera, V. Modafferi, S. Candamano, A. Donato, F. Frusteri and P. L. Antonucci, *Journal of Power Sources*, 2004, **135**, 177-183.

19. P. Bera, *Journal of Catalysis*, 2000, **196**, 293-301.

20. P. Bera, S. T. Aruna, K. C. Patil and M. S. Hegde, *Journal of Catalysis*, 1999, **186**, 36-44.

21. M. Nolan, S. C. Parker and G. W. Watson, *The journal of physical chemistry. B*, 2006, **110**, 2256-2262.

22. L. Kundakovic and M. Flytzani-Stephanopoulos, *Journal of Catalysis*, 1998, **179**, 203-221.

23. T. Zhu and M. Flytzani-Stephanopoulos, *Applied Catalysis A: General*, 2001, **208**, 403-417.

24. F. Yang, Y. Choi, S. Agnoli, P. Liu, D. Stacchiola, J. Hrbek and J. A. Rodriguez, *The Journal of Physical Chemistry C*, 2011, **115**, 23062-23066.

25. F. Yang, J. Graciani, J. Evans, P. Liu, J. Hrbek, J. F. Sanz and J. A. Rodriguez, *Journal of the American Chemical Society*, 2011, **133**, 3444-3451.

26. D. C. Sayle, S. A. Maicaneanu and G. W. Watson, *Journal of the American Chemical Society*, 2002, **124**, 11429-11439.

27. M. Nolan, S. Grigoleit, D. C. Sayle, S. C. Parker and G. W. Watson, *Surface Science*, 2005, **576**, 217-229.

28. G. N. Vayssilov, Y. Lykhach, A. Migani, T. Staudt, G. P. Petrova, N. Tsud, T. Skala, A. Bruix, F. Illas, K. C. Prince, V. Matolin, K. M. Neyman and J. Libuda, *Nature materials*, 2011, **10**, 310-315.

29. Q. Yuan, H. H. Duan, L. L. Li, L. D. Sun, Y. W. Zhang and C. H. Yan, *Journal of colloid and interface science*, 2009, **335**, 151-167.

30. X.-S. Huang, H. Sun, L.-C. Wang, Y.-M. Liu, K.-N. Fan and Y. Cao, *Applied Catalysis B: Environmental*, 2009, **90**, 224-232.

31. H. X. Mai, L. D. Sun, Y. W. Zhang, R. Si, W. Feng, H. P. Zhang, H. C. Liu and C. H. Yan, *The journal of physical chemistry. B*, 2005, **109**, 24380-24385.

32. Tana, M. Zhang, J. Li, H. Li, Y. Li and W. Shen, *Catalysis Today*, 2009, **148**, 179-183.

33. L. Liu, Z. Yao, Y. Deng, F. Gao, B. Liu and L. Dong, *ChemCatChem*, 2011, **3**, 978-989.

34. X. Du, D. Zhang, L. Shi, R. Gao and J. Zhang, *The Journal of Physical Chemistry C*, 2012, **116**, 10009-10016.

35. G. Yi, Z. Xu, G. Guo, K.-i. Tanaka and Y. Yuan, *Chemical Physics Letters*, 2009, **479**, 128-132.

36. R. Si and M. Flytzani-Stephanopoulos, *Angew Chem Int Ed Engl*, 2008, **47**, 2884-2887.

37. D. Gamarra, A. L. Cámara, M. Monte, S. B. Rasmussen, L. E. Chinchilla, A. B. Hungría, G. Munuera, N. Gyorffy, Z. Schay, V. C. Corberán, J. C. Conesa and A. Martínez-Arias, *Applied Catalysis B: Environmental*, 2013, **130-131**, 224-238.

38. P. Gawade, B. Mirkelamoglu and U. S. Ozkan, *The Journal of Physical Chemistry C*, 2010, **114**, 18173-18181.

39. R. Si, J. Raitano, N. Yi, L. Zhang, S.-W. Chan and M. Flytzani-Stephanopoulos, *Catalysis Today*, 2012, **180**, 68-80.

40. A. Martínez-Arias, M. Fernández-García, V. Ballesteros, L. N. Salamanca, J. C. Conesa, C. Otero and J. Soria, *Langmuir*, 1999, **15**, 4796-4802.

41. P. J. Chupas, K. W. Chapman, C. Kurtz, J. C. Hanson, P. L. Lee and C. P. Grey, *Journal of Applied Crystallography*, 2008, **41**, 822-824.

42. A. P. Hammersley, S. O. Svensson, M. Hanfland, A. N. Fitch and D. Hausermann, *High Pressure Research*, 1996, **14**, 235-248.

43. B. H. Toby, *Journal of Applied Crystallography*, 2001, **34**, 210-213.

44. A. C. Larson and R. B. V. Dreele, *Los Alamos National Laboratory: Report LAUR*, 2000, 86-748.

45. B. Ravel and M. Newville, *Journal of synchrotron radiation*, 2005, **12**, 537-541.

46. N. S. Marinkovic, Q. Wang and A. I. Frenkel, *Journal of synchrotron radiation*, 2011, **18**, 447-455.

47. O. Sipr, A. Simunek, S. Bocharov, T. Kirchner and G. Dräger, *Journal of Synchrotron Radiation*, 2001, **8**, 235-237.

48. N. Koizumi, S. Suzuki, Y. Ibi, Y. Hayasaka, Y. Hamabe, T. Shindo and M. Yamada, *Journal of synchrotron radiation*, 2012, **19**, 74-83.

49. C. Binet, M. Daturi and J.-C. Lavalley, *Catalysis Today*, 1999, **50**, 207-225.

50. A. Martínez-Arias, M. Fernández-García, J. Soria and J. C. Conesa, *Journal of Catalysis*, 1999, **182**, 367-377.

51. D. Gamarra, M. Fernández-García, C. Belver and A. Martínez-Arias, *The Journal of Physical Chemistry C*, 2010, **114**, 18576-18582.

52. G. N. Vayssilov, M. Mihaylov, P. St. Petkov, K. I. Hadjiivanov and K. M. Neyman, *The Journal of Physical Chemistry C*, 2011, **115**, 23435-23454.

53. K. Mudiyanselage, S. D. Senanayake, L. Feria, S. Kundu, A. E. Baber, J. Graciani, A. B. Vidal, S. Agnoli, J. Evans, R. Chang, S. Axnanda, Z. Liu, J. F. Sanz, P. Liu, J. A. Rodriguez and D. J. Stacchiola, *Angewandte Chemie International Edition*, 2013, **52**, 5101-5105.

54. M. Monte, D. Gamarra, A. López Cámara, S. B. Rasmussen, N. Gyorffy, Z. Schay, A. Martínez-Arias and J. C. Conesa, *Catalysis Today*, 2014, **229**, 104-113.

55. P. Liu and J. A. Rodriguez, *The Journal of chemical physics*, 2007, **126**, 164705.

56. J. L. Fajin, F. Illas and J. R. Gomes, *The Journal of chemical physics*, 2009, **130**, 224702.

57. Z. Yang, Q. Wang and S. Wei, *Physical chemistry chemical physics : PCCP*, 2011, **13**, 9363-9373.

58. D. R. Mullins, P. M. Albrecht, T.-L. Chen, F. C. Calaza, M. D. Biegalski, H. M. Christen and S. H. Overbury, *The Journal of Physical Chemistry C*, 2012, **116**, 19419-19428.

59. S. Fuente, M. M. Branda and F. Illas, *Theoretical Chemistry Accounts*, 2012, **131**.

This journal is © The Royal Society of Chemistry 2012

Phys. Chem. Chem. Phys., 2012, **00**, 1-3 | **13**